J|A|C|S
ARTICLES
Published on Web 03/03/2004

Electronic and Spectroscopic Studies of the Non-Heme Reduced Binuclear Iron Sites of Two Ribonucleotide Reductase Variants: Comparison to Reduced Methane Monooxygenase and Contributions to O_2 Reactivity

Pin-pin Wei,[†] Andrew J. Skulan,[†] Natasa Mitić,[†] Yi-Shan Yang,[†,§] Lana Saleh,[‡] J. Martin Bollinger, Jr.,*[,‡] and Edward I. Solomon*[,†]

Contribution from the Department of Chemistry, Stanford University, Stanford, California 94305, and Department of Biochemistry and Molecular Biology, Pennsylvania State University, University Park, Pennsylvania 16802

Received July 22, 2003; E-mail: edward.solomon@stanford.edu

Abstract: Circular dichroism (CD), magnetic circular dichroism (MCD), and variable-temperature variable-field (VTVH) MCD have been used to probe the biferrous active site of two variants of ribonucleotide reductase. The aspartate to glutamate substitution (R2-D84E) at the binuclear iron site modifies the endogenous ligand set of ribonucleotide reductase to match that of the binuclear center in the hydroxylase component of methane monooxygenase (MMOH). The crystal structure of chemically reduced R2-D84E suggests that the active-site structure parallels that of MMOH. However, CD, MCD, and VTVH MCD data combined with spin-Hamiltonian analysis of reduced R2-D84E indicate a different coordination environment relative to reduced MMOH, with no μ-(1,1)(η^1,η^2) carboxylate bridge. To further understand the variations in geometry of the active site, which lead to differences in reactivity, density functional theory (DFT) calculations have been carried out to identify active-site structures for R2-wt and R2-D84E consistent with these spectroscopic data. The effects of varying the ligand set, positions of bound and free waters, and additional protein constraints on the geometry and energy of the binuclear site of both R2-wt and variant R2s are also explored to identify the contributions to their structural differences and their relation to reduced MMOH.

Introduction

There has been considerable interest in understanding the chemistry of binuclear non-heme iron proteins, in particular, methane monooxygenase (MMO),[1−4] ribonucleotide reductase (RNR),[5,6] and stearoyl-acyl carrier protein Δ^9 desaturase (Δ^9D).[7−9] Although they perform distinctly different chemistries with dioxygen, the ligand sets of the binuclear ferrous active sites of these proteins are nearly identical and the clusters are structurally similar.[10] RNR utilizes a high-valent ($Fe^{III}Fe^{IV}$) iron−oxo intermediate (**X**) to form a stable tyrosine radical, which initiates the reduction of ribonucleotides to deoxyribonucleotides, while a high-valent ($Fe^{IV}Fe^{IV}$) iron−oxo intermediate (**Q**) of MMO cleaves the C−H bond of methane to convert it to methanol.[11,12] Despite this difference in reactivity, crystal structures (Figure 1A,C) of the reduced binuclear iron active sites of RNR (R2) and MMO (MMOH) have the same coordinating endogenous ligand set with the exception of the Asp84 in R2 versus the Glu114 in MMOH.[13,14]

Recently, there has been interest in engineering the site of ribonucleotide reductase to resemble that of methane monooxygenase to evaluate whether R2 might be able to perform chemistry similar to that performed by MMOH. Bollinger et al.[15] have reported that R2-D84E (also referred to as "single variant") generates a peroxo-level intermediate with $t_{1/2} = 0.75$ s at 5 °C. The Mössbauer and optical spectra of this intermediate resemble those of MMOH intermediate **P**.[16] However, no **P**-like peroxodiiron(III) complex has been observed in R2-wt.[17] R2-W48F/D84E (also referred to as "double variant") contains an

[†] Stanford University.
[‡] Pennsylvania State University.
[§] Current address: Lucas MRS Center, Department of Radiology, Stanford University Medical School, Stanford, CA 94305.

(1) Wallar, B. J.; Lipscomb, J. D. *Chem. Rev.* **1996**, *96*, 2625−2657.
(2) Merkx, M.; Kopp, D.; Sazinsky, M.; Blazyk, J.; Muller, J.; Lippard, S. J. *Angew. Chem., Int. Ed.* **2001**, *40*, 2782−2807.
(3) Baik, M. H.; Newcomb, M.; Friesner, R. A.; Lippard, S. J. *Chem. Rev.* **2003**, *103*, 2385−2420.
(4) Liu, Y.; Nesheim, J. C.; Paulsen, K. E.; Stankovich, M. T.; Lipscomb, J. D. *Biochemistry* **1997**, *36*, 5223−5233.
(5) Stubbe, J.; Nocera, D. G.; Yee, C. S.; Chang, M. C. *Chem. Rev.* **2003**, *103*, 2167−2202.
(6) Yang, Y. S.; Baldwin, J.; Ley, B. A.; Bollinger, J. M., Jr.; Solomon, E. I. *J. Am. Chem. Soc.* **2000**, *122*, 8495−8510.
(7) Shanklin, J.; Cahoon, E. B. *Annu. Rev. Plant Physiol. Plant Mol. Biol.* **1998**, *49*, 611−641.
(8) Solomon, E. I.; Brunold, T. C.; Davis, M. I.; Kemsley, J. N.; Lee, S. K.; Lehnert, N.; Neese, F.; Skulan, A. J.; Yang, Y. S.; Zhou, J. *Chem. Rev.* **2000**, *100*, 235−349.
(9) Yang, Y. S.; Broadwater, J. A.; Pulver, S. C.; Fox, B. G.; Solomon, E. I. *J. Am. Chem. Soc.* **1999**, *121*, 2770−2783.
(10) Nordlund, P.; Eklund, H. *Curr. Opin. Struct. Biol.* **1995**, *5*, 758−766.
(11) Liu, K. E.; Valentine, A. M.; Wang, D. L.; Huynh, B. H.; Edmondson, D. E.; Salifoglou, A.; Lippard, S. J. *J. Am. Chem. Soc.* **1995**, *117*, 10174−10185.
(12) Fox, B. G.; Liu, Y.; Dege, J. E.; Lipscomb, J. D. *J. Biol. Chem.* **1991**, *266*, 540−550.
(13) R2 is the subunit of RNR that contains the binuclear iron active site. MMOH is the hydroxylase component of MMO.
(14) Whittington, D. A.; Lippard, S. J. *J. Am. Chem. Soc.* **2001**, *123*, 827−838.
(15) Bollinger, J. M., Jr.; Krebs, C.; Vicol, A.; Chen, S.; Ley, B. A.; Edmondson, D. E.; Huynh, B. H. *J. Am. Chem. Soc.* **1998**, *120*, 1094−1095.

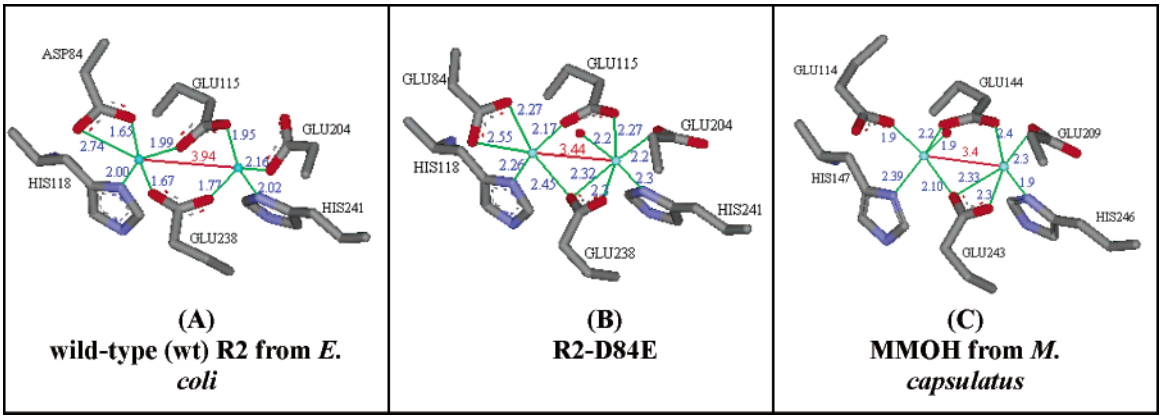

Figure 1. (A−C) Crystal structures of the reduced binuclear active site of (A) R2-wt (1XIK), (B) R2-D84E, and (C) MMOH. The R2-D84E and MMOH structures were generated using PDB files from ref 21 for R2-D84E and ref 22 for MMOH.

additional phenylalanine substitution at the W48 site, which has been implicated in the electron-transfer chain between the binuclear iron site and the R1 catalytic site and has been shown to shuttle an electron to the diiron site during O_2 activation.[18] This double variant forms a peroxo-level intermediate with $t_{1/2}$ = 2.7 s at 5 °C and is observed to self-hydroxylate at F208 upon exposure to O_2.[19]

Crystal structures of reduced wild-type (R2-wt), R2-D84E, and MMOH have been reported and are shown in Figure 1.[20−22] The structure of the R2-wt from *E. coli* shows two four-coordinate (4C) irons bridged by two carboxylate ligands in a μ-1,3 fashion (Figure 1A).[23] Alternatively, MCD spectroscopy identifies a four- and five-coordinate (4C+5C) biferrous species.[24] Possible explanations for the differences between the spectroscopy and crystallography are as follows: E204 is disordered in the crystal structure and could be bidentate in solution; a solvent-derived ligand with low electron density could also be present;[25] or the different sample preparation conditions required for crystallization could result in a different coordination geometry from that in the MCD samples. The crystal structure obtained from the reduced R2-D84E variant presents an active site remarkably similar to that in MMOH (Figure 1B vs 1C).[21] In this variant, the irons in the binuclear site are 5C+6C bridged by two carboxylate ligands: E115 in a μ-1,3 configuration and E238 in a μ-1,1(η^1,η^2) fashion[26] (bidentate to Fe2). These modes parallel those of the carboxylate bridges found in MMOH.[22,27]

Quantum chemistry studies on the biferrous active sites of MMOH[28−30] and R2 [29−31] have achieved varying degrees of fidelity in reproducing the geometries obtained crystallographically, depending on the theoretical approach used (DFT or combined QM/MM methods) and the size of the model. In one case,[28] this resulted in modification of previously published crystallographic data.[22] Calculations reproducing the active-site coordination geometry require a DFT-level description of the biferrous unit and complete coordinated amino acid R-groups. Coordinated amino acids need to be constrained by either the protein backbone[32,33] or a frozen α-carbon coordinate to model this geometric limitation.[28] Additional interactions between the coordinating residues and specific hydrogen-bonded second-coordination-sphere residues must also be modeled, as they show significant protein-field interaction energies[32,33] and their absence decreases the correlation of calculated structures with the known geometric and spectroscopic features of these sites.[28,34]

This study utilizes near-IR CD and MCD spectroscopies to probe excited states and VTVH MCD data to define the ground state in R2-D84E and R2-W48F/D84E. Crystallographic studies have different preparation methods from those used in kinetic and spectroscopic studies, and this difference may be responsible for the discrepancies in coordination geometry deduced from each method.[27,35] CD and MCD in the near-IR region can directly probe the d → d transitions and, thus, deduce the nature of the ligation of each iron of the binuclear Fe^{II} site.[36] Past studies have shown that a 6C high-spin Fe(II) has two d → d transitions around ∼10 000 cm^{-1} split by up to ∼2000 cm^{-1}. Removing a ligand to become five-coordinate splits these transitions, giving two features around 5000 and 10 000 cm^{-1}. For a 4C tetrahedral Fe^{II} site, the low energy d → d transitions are observed in the region of ∼5000 to ∼7000 cm^{-1}. The

(16) **P** is also referred to in the literature as H_{peroxo}.
(17) Sturgeon, B. E.; Burdi, D.; Chen, S. X.; Huynh, B. H.; Edmondson, D. E.; Stubbe, J.; Hoffman, B. M. *J. Am. Chem. Soc.* **1996**, *118*, 7551−7557.
(18) Krebs, C.; Chen, S. X.; Baldwin, J.; Ley, B. A.; Patel, U.; Edmondson, D. E.; Huynh, B. H.; Bollinger, J. M., Jr. *J. Am. Chem. Soc.* **2000**, *122*, 12207−12219.
(19) Baldwin, J.; Voegtli, W. C.; Khidekel, N.; Moenne-Loccoz, P.; Krebs, C.; Pereira, A. S.; Ley, B. A.; Huynh, B. H.; Loehr, T. M.; Riggs-Gelasco, P. J.; Rosenzweig, A. C.; Bollinger, J. M., Jr. *J. Am. Chem. Soc.* **2001**, *123*, 7017−7030.
(20) Logan, D. T.; Su, X.-D.; Åberg, A.; Regnström, K.; Hajdu, J.; Eklund, H.; Nordlund, P. *Structure* **1996**, *4*, 1053−1064.
(21) Voegtli, W. C.; Khidekel, N.; Baldwin, J.; Ley, B. A.; Bollinger, J. M., Jr.; Rosenzweig, A. C. *J. Am. Chem. Soc.* **2000**, *122*, 3255−3261.
(22) Rosenzweig, A. C.; Nordlund, P.; Takahara, P. M.; Frederick, C. A.; Lippard, S. J. *Chem. Biol.* **1995**, *2*, 409−418.
(23) Both His118 and His241 are monodentate on all structures described and remain so for the rest of this paper.
(24) Pulver, S. C.; Tong, W. H.; Bollinger, J. M., Jr.; Stubbe, J.; Solomon, E. I. *J. Am. Chem. Soc.* **1995**, *117*, 12664−12678.
(25) Logan, D. T.; deMare, F.; Persson, B. O.; Slaby, A.; Sjoberg, B. M.; Nordlund, P. *Biochemistry* **1998**, *37*, 10798−10807.
(26) μ-1,1(η^1,η^2) indicates that both irons are bridged by the same oxygen on the carboxylate which binds in a bidentate fashion to one Fe.
(27) Whittington, D. A.; Lippard, S. J. *J. Am. Chem. Soc.* **2001**, *123*, 827−838.
(28) Dunietz, B. D.; Beachy, M. D.; Cao, Y. X.; Whittington, D. A.; Lippard, S. J.; Friesner, R. A. *J. Am. Chem. Soc.* **2000**, *122*, 2828−2839.
(29) Torrent, M.; Musaev, D. G.; Basch, H.; Morokuma, K. *J. Comput. Chem.* **2002**, *23*, 59−76.
(30) Lovell, T.; Han, W. G.; Liu, T. Q.; Noodleman, L. *J. Am. Chem. Soc.* **2002**, *124*, 5890−5894.
(31) Torrent, M.; Musaev, D.; Morokuma, K. *J. Phys. Chem. B* **2001**, *105*, 322−327.
(32) Lovell, T.; Li, J.; Noodleman, L. *Inorg. Chem.* **2001**, *40*, 5267−5278.
(33) Lovell, T.; Li, J.; Noodleman, L. *J. Biol. Inorg. Chem.* **2002**, *7*, 799−809.
(34) Siegbahn, P. E. M.; Crabtree, R. H.; Nordlund, P. *J. Biol. Inorg. Chem.* **1998**, *3*, 314−317.
(35) Voegtli, W. C.; Sommerhalter, M.; Saleh, L.; Baldwin, J.; Bollinger, J. M., Jr.; Rosenzweig, A. C. *J. Am. Chem. Soc.* **2003**, *125*, 15822−15830.
(36) Solomon, E. I.; Pavel, E. G.; Loeb, K. E.; Campochiaro, C. *Coord. Chem. Rev.* **1995**, *144*, 369−460.

temperature and magnetic field dependence of the MCD signals (VTVH MCD) can further be used to obtain detailed information about the energy splittings of the ground-state sublevels. Sublevel energies obtained from the spin-Hamiltonian analysis of the VTVH MCD data give the exchange coupling (J) and zero-field splitting (D) values, where D probes each Fe^{II} site geometry and J gives insight into the nature of the bridging ligands.

The results from spectroscopy are related to the active-site geometries of wt and the single and double variant R2s using quantum chemical modeling of the active sites of these two proteins. This identifies structural features which lead to the spectroscopic features observed. These spectroscopic/DFT studies provide insight into the geometric and electronic differences among the R2-D84E variants, R2-wt and MMOH. This gives a better understanding of the structural differences correlating to their functional diversity in O_2 reactivity.

Experimental Section

I. Spectroscopic Studies. Hepes buffer (Sigma), sodium chloride (Sigma), ferrous ammonium sulfate hexahydrate (Mallinckroft), deuterium oxide (99.9 atom % D, Aldrich), sodium dithionite (Aldrich), and d_3-glycerol (98 atom % D, Cambridge Isotope Laboratories) were commercially purchased and used as obtained. Deuterated buffer was degassed with 99.9% pure argon; d_3-glycerol was degassed by heating under vacuum overnight and then finished with at least 10 freeze−pump−thaw cycles at 10^{-3} Torr. Protein samples were degassed by rapidly purging with at least 10 vacuum/argon cycles; solid ferrous ammonium sulfate was pumped at 10^{-3} KPa for at least 1 h. The protein samples were prepared and loaded into the sample holder in an inert atmosphere.

R2-wt, R2-D84E,[37] and R2-W48F/D84E[21] were expressed and purified as previously reported. The protein concentration for the wild-type and single variant was determined by using the molar extinction coefficient $\epsilon_{280} = 120$ mM^{-1} cm^{-1}/R2-dimer. The molar extinction coefficient of R2-W48F/D84E is 109.24 mM^{-1} cm^{-1}/dimer, corrected from the value for R2-wt according to the method of Gill and von Hippel.[38] Buffer exchange was carried out by diluting 150 μL of 2 mM apo protein with deuterated buffer (0.15 M Hepes, pD 7.6) and reconcentrating back to 2 mM by ultrafiltration (Amicon stirred YM30 ultrafiltration cell, Beverly, MA). This process was repeated until the percentage of D_2O was greater than 99.9% of the solvent.

The degassed apoprotein was fully reduced with 1.5 μL of 5 mM methyl viologen and 2 μL of 10 mM dithionite before the ferrous solution was added to fully load the iron center. The appropriate amount of the ferrous ion solution was added anaerobically to the apoprotein and incubated for 10 min. The sample was transferred to an anaerobic cuvette for CD measurements. CD spectra showed no noticeable change with the addition of glycerol. Protein samples were prepared for MCD in the same way as for CD with an additional step of manually mixing the protein with 60% (v/v) glycerol-d_6 pD 7.8 until homogeneous to create a suitable glass. The samples were then immediately frozen in liquid nitrogen.

CD studies were performed on a JASCO J200D spectropolarimeter operating with a liquid nitrogen-cooled InSb detector in the 560−2000 nm region. Low-temperature MCD data were acquired on this spectropolarimeter, modified to accommodate an Oxford Instrument SM4000-7T superconducting magnet capable of magnetic fields up to 7.0 T and temperatures down to 1.6 K. Protein samples prepared for MCD studies were slowly inserted into the cryostat to reduce strain in the resulting optical glass.

(37) Moenne-Loccoz, P.; Baldwin, J.; Ley, B. A.; Loehr, T. M.; Bollinger, J. M., Jr. *Biochemistry* **1998**, *37*, 14659−14663.
(38) Gill, S. C.; von Hippel, P. H. *Anal. Biochem.* **1989**, *182*, 319−326.

The baseline-corrected CD and MCD spectra were fit using a constrained nonlinear least-squares procedure. Each spectroscopic method has a different selection rule; thus, transitions can have different intensities and signs but similar energies. The MCD spectra are taken at low temperature; thus, they may have significantly sharper bandwidths, and the band energies may shift slightly relative to the room-temperature CD data, which were allowed to float in the final fit. VTVH MCD data (MCD intensity, temperature, and applied magnetic field) were fit using a simplex routine that minimizes the χ-squared value. A goodness of fit parameter (χ-square/number of float parameters) was utilized in the comparison of different fit results. In addition, a spin-projection model was applied to confirm the results obtained from the simplex routine (doublet model) and identify the specific Fe center of the dimer associated with the ligand field transition being studied by VTVH MCD.

II. Density Functional Calculations. Electronic structure calculations were performed on an SGI 2000 computer using version 4.1 of the Jaguar quantum chemistry software. All calculations were performed using the local density approximation of Vosko, Wilk, and Nusair for exchange and correlation[39] and the nonlocal gradient corrections of Becke and Perdew.[40−42] The biferrous calculations presented in this manuscript are a precursor to a spectroscopic and computational study of the peroxo-level intermediate in R2-wt and R2-W48F/D84E.[43] Geometry optimizations were performed on models of the R2 active site based upon the R2-W48F/D84E and R2-wt crystal structures, 1PJO and 1PIY, respectively. The structures were considered optimized when meeting the default geometry optimization criteria of Jaguar 4.1.[44] The model chosen for the R2 active site includes the six coordinating residues (D/E84, E115, H118, E204, E238, H241) truncated at the α-carbon position[45] and analogues of the principle residues involved in hydrogen-bonding to the coordinating residues (Q43, Q87, W111, S114, Y122, D237).[46] This resulted in a model consisting of 93 (W48F/D84E) and 87 (wt) atoms (representative pictures of the R2-W48F/D84E model found in Supporting Information S1).[47] The H-bonding residues included correlate well with those identified as having strong interactions with the six iron-coordinating residues from combined QM/MM calculations.[33] For geometry optimizations, the iron atoms were described by the LACVP* double-ζ basis set;[48] atoms within three bonds of the iron atoms used 6-31G*, and all others used 6-31G. The basis set size was increased to triple-ζ for determining energies, with

(39) Vosko, S. H.; Wilk, L.; Nusair, M. *Can. J. Phys.* **1980**, *58*, 1200.
(40) Becke, A. D. *J. Chem. Phys.* **1986**, *84*, 4524.
(41) Perdew, J. P. *J. Chem. Phys.* **1986**, *33*, 8822.
(42) BP86 was selected as the functional in this investigation as there is a good correlation between the electronic structure of biferric peroxo complexes and that predicted by BP86 calcuations (Brunold, T. C.; et al. *J. Am. Chem. Soc.* **1998**, *120*, 5674−5690).
(43) Skulan, A. J., manuscript in preparation.
(44) Geometry convergence criteria were as follows: change in total energy, $\Delta E < 5e{-}5$ hartrees, maximum local energy gradient, $\delta E/\delta S < 4.5e{-}4$ hartrees/Å, $\delta E/\delta S$(RMS) $< 3e{-}4$ hartrees/Å, $\Delta S < 1.8e{-}3$ Å, ΔS(RMS) $< 1.2e{-}5$ Å. Frequency calculations to verify that true minima had been attained were not possible as Jaguar 4.1 and subsequent Jaguar 5.0 have not implemented parallelized analytical frequency determination. Such calculations will be performed once this functionality has been added.
(45) The residue truncation was performed as follows: the α-carbon was replaced by a hydrogen atom with concomitant shortening of the α-C−β-C bond to 1.08 Å, with the β-C retaining its original position. This hydrogen was then frozen in all geometry optimizations.
(46) The hydrogen-bonding residues were truncated to the smallest reasonable models providing hydrogen-bonding interactions similar to those observed in the protein. These were as follows: Q43; formamide, $COHNH_2$, Q87; ammonia, NH_3, W111; ammonia, NH_3, S114; water, H_2O, Y122; water, H_2O, D237; formate, CHO_2^-. The positions of the heavy atoms (C, N, O) were frozen along with the positions of hydrogens replacing carbon atoms. Q43 and Q87 were modeled differently (as formamide and ammonia, respectively) as the R-group nitrogen of Q43 was located 2.8 Å from a carboxylate oxygen on D237 suggesting hydrogen bonding between these two residues which may have been of importance to the geometry of the active site. W/F48 residue, the second substitution from wt, was not included in the model as it does not coordinate to either iron or iron-coordinated residues.
(47) The atom count differs between the two calculations due to the addition of a methylene ($-CH_2-$) by the D84E substitution and the introduction of a water molecule which is hydrogen-bonded to E84 in the variant.
(48) Hay, P. J.; Wadt, W. R. *J. Chem. Phys.* **1985**, *82*, 299−310.

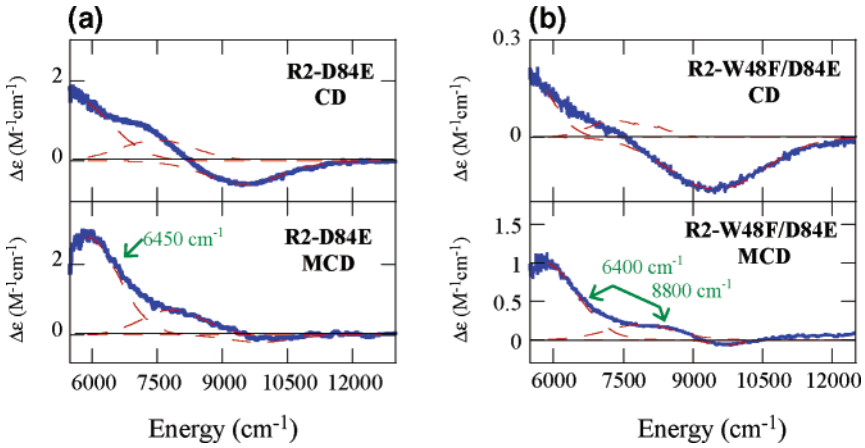

Figure 2. CD (top) and MCD (bottom) of R2-D84E (a) and R2-W48F/D84E (b). Green arrows indicate the energy position used for the VTVH data in Figures 5 and 6.

the LACV3P* basis used for Fe, 6-311G* used for atoms within three bonds of the iron atoms, and 6-311G used for all other atoms.

Results and Analysis

I. NIR CD/MCD and Excited-State Analysis. (a) CD/MCD of Reduced R2-D84E and R2-W48F/D84E. CD/MCD[49] spectra of the reduced, iron-loaded R2-D84E and R2-W48F/D84E are shown in Figure 2a and 2b, respectively. Dashed lines are used for the Gaussian fit in each case. R2-D84E shows three bands at 10 000, 7800, and 5900 cm^{-1}. R2-W48F/D84E also shows three bands at 10 000, 7800, and 5900 cm^{-1} which almost overlay those of the single variant. The ligand field transitions of the two irons remain the same, as the W48F substitution does not directly involve the iron ligands. Further addition of ferrous ion leads to two positive MCD transitions growing in around 10 000 cm^{-1}. These are assigned to free aqueous iron and are not observed in the CD because this species is achiral.

The presence of three transitions in the NIR region indicates that the two Fe(II) atoms in the metal binding site have different coordination environments, because a single Fe(II) atom cannot have more than two ligand field transitions above 5000 cm^{-1}. The presence of only one transition above 8000 cm^{-1} in the CD/MCD spectra indicates that neither iron is 6C.[50] Thus, the band at 10 000 cm^{-1} for the single and double variants must be associated with a 5C iron, while the lower energy transitions at 7800 and 5900 cm^{-1} reflect a 4C site. The CD and MCD data for the single and double variants in Figure 2 are very similar, showing that the binuclear center is not substantially affected by the W48F substitution. The CD (top) and MCD (bottom) spectra of the R2-wt (black), R2-D84E (blue), and MMOH (red) are shown in Figure 3.[51] The CD spectrum of R2-wt is comparable to that of the single variant and exhibits three transitions at ~9000, 7500, and 5500 cm^{-1}. There are, however, intensity differences between their MCD spectra. The single variant exhibits an intensity ratio of 3:1 (I(5500 cm^{-1})/I(7500 cm^{-1})), while R2-wt exhibits a 1:3 ratio. Both variants and R2-wt exhibit transitions which indicate the sites are 4C+5C binuclear centers. In contrast, the CD/MCD spectra of reduced MMOH have peaks at 7550, 9100, and 9900 cm^{-1}. These are

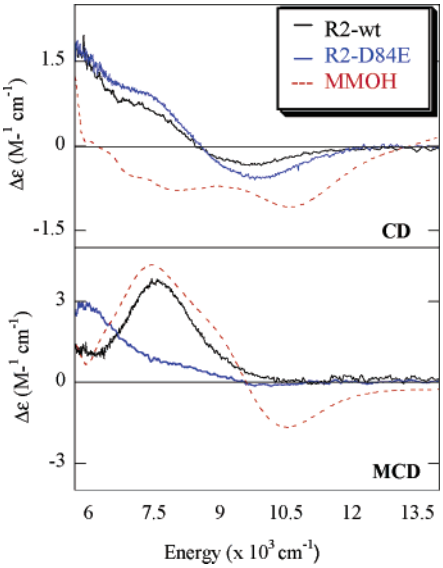

Figure 3. CD (top) and MCD (bottom) of the R2-wt, R2-D84E, and MMOH.

different from the features of reduced R2-wt and R2-D84E and indicate the presence of two five-coordinate iron centers.[52]

(b) Chemical Perturbations. Because the spectroscopy does not agree with the coordination environment obtained by crystallographic studies on the single variant,[21] experiments were conducted to evaluate chemical differences which could cause the 4C+5C site to become 5C+6C. Preparation of crystals of ferrous R2-D84E involved chemically reducing the crystalline diiron(III) protein in a solution of 200 mM NaCl. Sodium dithionite was used as the chemical reducing agent, and the final pH was reported to be 5.0.[21] Previous MCD studies[6] found that the presence of chloride and varying pH can significantly alter the spectrum of R2-wt. Therefore, we tested whether the method of preparation of the reduced R2-D84E protein in solution affects the CD/MCD spectra and deduced coordination geometry. Neither the CD nor the MCD reveal any discernible difference between the reduced protein prepared by iron loading of the apo protein and that prepared by chemical reduction of the diiron(III) form (Figure 4). MCD spectra of the chemically reduced versus Fe(II) loaded R2-wt are provided in Supporting

(49) CD was taken on a solution at 5 °C while MCD data were taken on a glass at 1.6 K.
(50) Solomon, E. I.; Pavel, E. G.; Loeb, K. E.; Campochiaro, C. *Coord. Chem. Rev.* **1995**, *144*, 369−460.
(51) Because the CD/MCD of the R2-W48F/D84E are almost the same as the single variant, they are not included for clarity.
(52) Pulver, S.; Froland, W. A.; Fox, B. G.; Lipscomb, J. D.; Solomon, E. I. *J. Am. Chem. Soc.* **1993**, *115*, 12409−12422.

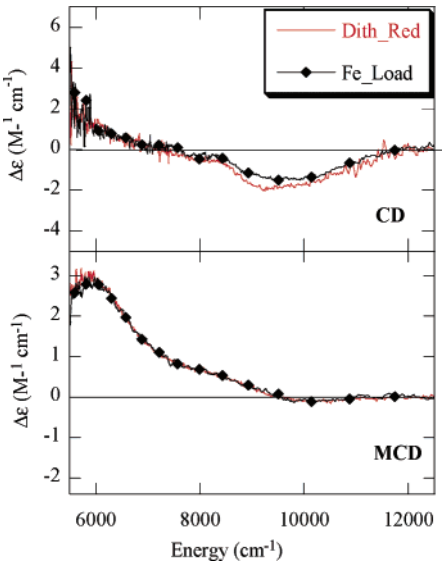

Figure 4. CD and MCD of dithionite reduced (red) and Fe-loaded (black line with diamonds) R2-D84E.

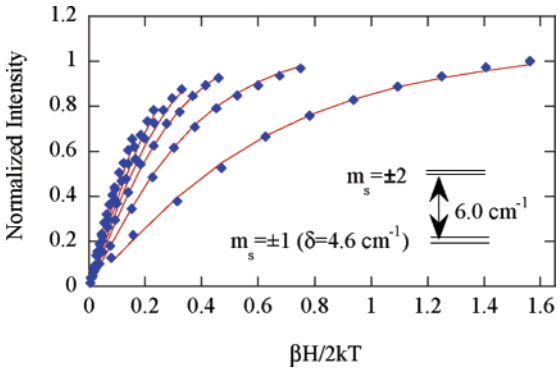

Figure 5. VTVH of reduced R2-D84E taken at 6450 cm^{-1}. The intensity amplitude (diamonds) for a range of magnetic fields (0−7.0 T) at a series of fixed temperatures is plotted as a function of βH/2kT.

Information S4. The spectrum of a sample with a salt concentration of 200 mM overlays the original spectrum within the standard deviation. No spectra could be collected at pH = 5.0, as the protein precipitated out of solution at a pH of 6.0.

II. Variable-Temperature Variable-Field (VTVH) MCD and Ground-State Analysis. The MCD intensity of reduced R2-D84E increases as temperature decreases, indicating that these transitions are MCD *C*-terms associated with paramagnetic doublets that are split by a magnetic field. By analyzing the ground state of the binuclear center, one can gain further insight into the Fe coordination and nature of the bridging ligands. Figure 5 shows the VTVH MCD saturation-magnetization curves of reduced R2-D84E taken at 6450 cm^{-1} (see green arrow in Figure 2A). The VTVH curves are nested, with the high-temperature data offset from the low-temperature data when the isotherms are plotted as a function of βH/2kT. This is characteristic of rhombic zero-field splitting (ZFS) of a non-Kramers doublet ground state and arises from nonlinear field-induced mixing between the sublevels of the doublet. Due to the low intensity and overlap with the peak at 5500 cm^{-1}, satisfactory VTVH data could not be collected at ~8000 cm^{-1} in MCD for the single variant. VTVH MCD data were collected at both 6400 and 8000 cm^{-1} for the double variant (Figure 2B, green arrows). The VTVH data at 8800 cm^{-1} are shown in

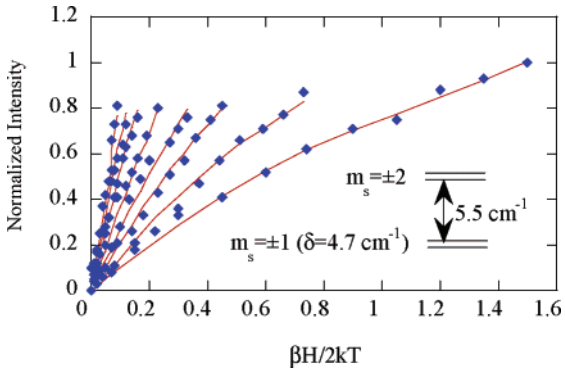

Figure 6. VTVH of R2-W48F/D84E taken at 8800 cm^{-1}. Best fit line (red) is overlaid on the data (blue diamonds).

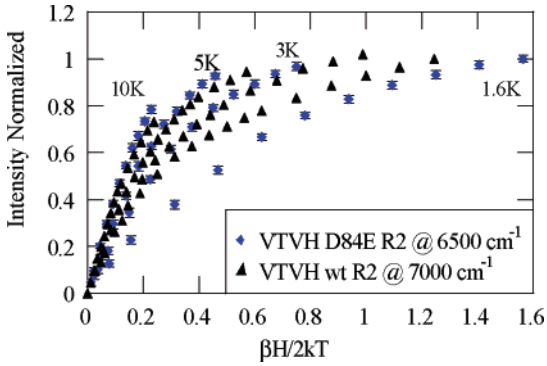

Figure 7. VTVH overlay of wt R2 (black triangles) and R2-D84E (blue diamonds).

Figure 6.[53] The VTVH data for R2-D84E and R2-wt are similar, but do not overlay within standard deviation. This is shown in Figure 7 (R2-wt in black, R2-D84E in blue).

The VTVH MCD data for the single variant were fit using the MCD intensity expression for a non-Kramers system, allowing for the effects of a linear *B*-term from field-induced mixing between states and the presence of excited sublevels of the ground state, as shown by eq 1 below:[50,54−57]

$$\Delta\epsilon = \sum_i \left[(A_{\mathrm{satlim}})_i \left(\int_0^{\frac{\pi}{2}} \frac{\cos^2\theta \sin\theta}{\Gamma_i} g_{\parallel i} \beta H \alpha_i \, d\theta - \sqrt{2}\frac{M_z}{M_{xy}} \int_0^{\frac{\pi}{2}} \frac{\sin^3\theta}{\Gamma_i} g_{\perp i} \beta H \alpha_i \, d\theta \right) + B_i H \gamma_i \right] \quad (1)$$

where

$$\Gamma_i = \sqrt{\delta_i^2 + (g_{\parallel i}\beta H \cos\theta)^2 + (g_{\perp i}\beta H \sin\theta)^2}$$

$$\alpha_i = \frac{e^{-(E_i-\Gamma_i/2)/kT} - e^{-(E_i+\Gamma_i/2)/kT}}{\sum_j e^{-(E_j-\Gamma_j/2)/kT} + e^{-(E_j+\Gamma_j/2)/kT}}$$

$$\gamma_i = \frac{e^{-(E_i-\delta_i/2)/kT} + e^{-(E_i+\delta_i/2)/kT}}{\sum_j e^{-(E_j-\beta_j/2)/kT} + e^{-(E_j+\delta_j/2)/kT}}$$

$(A_{\mathrm{satlim}})_i$, B_i, δ_i, $g_{\parallel i}$, and $g_{\perp i}$ are the *C*-term and *B*-term MCD intensity, the rhombic ZFS, and the dimer *g* values of the *i*th doublet, respectively. E_i is the energy of the *i*th sublevel, and

Table 1. Summary of the VTVH Fit Parameters of Reduced R2-D84E and R2-W48F/D84E (R2-wt and MMOH Are Included for Comparison)

	R2-wt, 7700 cm^{-1}	R2-D84E, 6460 cm^{-1}	R2-W84F/D48E, 8818 cm^{-1}	MMOH, 7575.8 cm^{-1}
δ	4.6	4.6	4.7	$<\sim 1$
$g_{\|\|}$ (ground)	8	3.9	4	14.7
$g_{\|\|}$ (excited)	4	8	8	0
E (cm^{-1})	6	5.98	5.47	8
J (cm^{-1})	−0.44	−1.5	−1.5	+0.3−0.5
D (cm^{-1})	−10	−10	−10	−4
D (cm^{-1})	4	5	5	−10

the energy of the ground state is defined as zero. The Boltzmann population over all states has been included in both the *C*-term and the *B*-term intensities as the factors α_i and γ_i, respectively. *H* is the applied magnetic field, *k* is the Boltzmann constant, and M_z and $M_{x,y}$ are the transition dipole moments for the directions indicated.

The lowest temperature (1.6 K) data collected at 6450 cm^{-1} for the single variant in Figure 5 were fit using eq 1 by floating the A_{satlim}, *B*, δ, and $g_{||}$, while fixing $g_\perp$ and the polarization ratio $M_z/M_{x,y}$ at zero. The best fit to the complete data set requires a single non-Kramers doublet with $g_{||} = 4$ and $\delta = 4.6$ cm^{-1}, indicating that the ground state is $M_s = \pm 1$. Fits using $g_{||} = 8$, 12, or 16 were poor (graphically and goodness of fit), and an excited doublet at ~ 6 cm^{-1} above the ground state with $g_{||} = 8$ (i.e., $M_s = \pm 2$) is required to fit the higher-temperature saturation data. Fits with an excited-state energy above 13 cm^{-1} did not fall within the standard deviation of the data set, while fits with this excited doublet at 5 cm^{-1} or lower had slightly larger goodness of fit parameters, but still stayed within the error bars. Inclusion of a third state for either variant does not have a significant effect on the fitting results. Floating $g_\perp$ and $M_z/M_{x,y}$ did not improve the fit. The VTVH MCD data on the band at 6400 cm^{-1} of the R2-W48F/D84E overlay within standard deviation with the data for the 6450 cm^{-1} band of the R2-D84E (Supporting Information S2). A good fit for the 8800 cm^{-1} band of R2-W48F/D84E (Figure 6) gives a ground state of $M_s = \pm 1$ and an excited state of $M_s = \pm 2$ at 5.5 cm^{-1} above the ground state. The parameters obtained for R2-D84E and R2-W48F/D84E are given in Table 1. Included for comparison are the results for the R2-wt[24] (first column) and reduced MMOH[52] (last column). Note that R2-wt has a ground state with $g_{||} \approx 8$ corresponding to $M_s = \pm 2$, whereas MMOH has a ground-state sublevel $g_{||} \approx 16$ with $M_s = \pm 4$. Although the energy of the excited state for the single variant is nearly equal in magnitude as compared to the R2-wt, the spins of the ground and excited states have flipped.

To define the *J* and *D* values of this coupled binuclear system, a spin-Hamiltonian analysis was performed to correlate to the ground-state sublevels obtained in Table 1. Equation 2 gives a simplified expression for the spin-Hamiltonian of a general non-heme biferrous system, which operates on the uncoupled basis set $|S_1, S_2, M_{s1}, M_{s2}\rangle$, where the subscripts indicate the two ferrous centers:

$$H = -2J\hat{S}_1\cdot\hat{S} + D_1(\hat{S}_{z1}^2 - {}^1/_3S(S+1)) + E_1(\hat{S}_{x1}^2 - \hat{S}_{y1}^2) + D_2(\hat{S}_{z2}^2 - {}^1/_3S(S+1)) + E_2(\hat{S}_{x2}^2 - \hat{S}_{y2}^2) + g_{z1}\beta H_z\hat{S}_{z1} + g_{x1}\beta H_x\hat{S}_{x1} + g_{y1}\beta H_y\hat{S}_{y1} + g_{z2}\beta H_z\hat{S}_{z2} + g_{x2}\beta H_x\hat{S}_{x2} + g_{y2}\beta H_y\hat{S}_{y2} \quad (2)$$

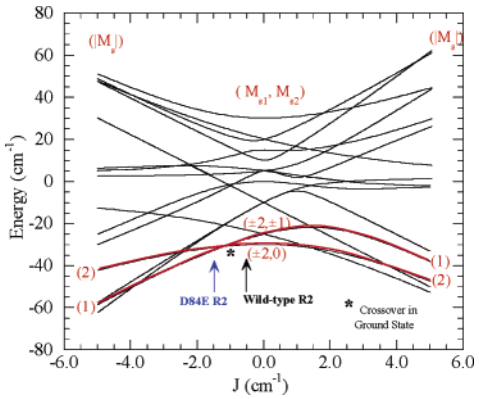

Figure 8. Correlation diagram of the energy levels of the binuclear ferrous ground state with $D_1 = +5$ cm^{-1} and $D_2 = -10$ cm^{-1}. The right side of the entire diagram indicates a ferromagnetic interaction ($J > 0$) between the ferrous atoms, and the left side indicates an antiferromagnetic interaction ($J < 0$). The ground state and first excited state for -2.5 $cm^{-1} < J < +0.5$ cm^{-1} is outlined in red.

where *J* is the exchange coupling between the two irons, D_1, D_2, E_1, and E_2 are the axial and rhombic ZFS parameters, and *H* is the magnetic field. Zeeman terms ($g_{z1}\beta H_{z1}S_{z1}$...etc.) are also included, where the *g* value can be coupled to the ZFS parameters using ligand field theory as given in eq 2a and 2b. λ is the Fe(II) ground-state spin−orbit coupling constant (~ 100 cm^{-1}), and k^2 is the Stevens orbital reduction factor, which is <1 and accounts for the effects of covalency.

$$D_{Fe^{2+}} = \frac{-k^2\lambda}{4}(g_{xFe^{2+}} + g_{yFe^{2+}} - 2g_{zFe^{2+}}) \quad (2a)$$

$$E_{Fe^{2+}} = \frac{-k^2\lambda}{4}(g_{yFe^{2+}} - g_{xFe^{2+}}) \quad (2b)$$

A high-spin ferrous ion has an $S = 2$ ground state with $M_s = 0$, ± 1, and ± 2. This 5-fold degeneracy will split due to zero-field splitting. In an exchange coupled system, the two ferrous ions can also interact through bridging ligands to give $S_{tot} = |S_1 + S_2|$ .... $|S_1 - S_2| = 4$, 3, 2, 1, and 0 levels. These levels are split by the exchange coupling $H = -2JS_1S_2$ to generate $(2S_{tot} + 1)M_s$ degenerate levels, which are further split in energy by zero-field splitting (ZFS). Because the magnitudes of *D* and *J* are comparable in binuclear non-heme ferrous systems, their combined effects need to be considered.

A 25 × 25 matrix is generated, and diagonalization of this matrix in zero magnetic field gives the wave functions of the binuclear ferrous spin states and their energies, which are dependent on the relative magnitudes and signs of the exchange coupling and the ZFS. The magnitude of the *D* values is constrained to be less than |15| cm^{-1} (the largest value observed in model systems and ligand field calculations); the maximum $|E/D|$ is $^1/_3$ by definition.

From Table 1, both variants have a ground state with $M_s = \pm 1$ and a lowest excited state of $M_s = \pm 2$. This situation can occur only with two *D* values of opposite signs. This is consistent with the 5C+4C structure deduced from CD and MCD analysis. Figure 8 gives a representative energy level diagram with $D_1 = +5$ cm^{-1} and $D_2 = -10$ cm^{-1}. The left side of the figure gives antiferromagnetic coupling ($J < 0$), which generates a ground state of (S_{tot}, $\pm M_s$) = (2, ±2), (1, ±1), or (0, ±0) as $-J$ increases.

Table 2. Spin-Hamiltonian Fitting of Reduced R2-D84E and R2-W48F/D84E

	R2-D84E	R2-W48F/D84E	
J (cm^{-1})	−1.5	−1.5	−1.5
D_1 (cm^{-1})	4.6	−10	5
D_2 (cm^{-1})	−10	5	−10
	axial	axial	rhombic
%x	0	16	5
%y	100	7	91
%z	0	77	4

From above, the ground state and first excited state for -2.0 $cm^{-1} < J < 0$ cm^{-1} are highlighted in red. Antiferromagnetic (negative J) coupling is shown on the left side of Figure 8, and the blue arrow points to the location of the R2 variants, while the position of R2-wt is shown by the black arrow.[52] The ground state flips from $M_s = \pm 2$ to $M_s = \pm 1$ as J becomes more negative. Thus, the change in ground state between R2-wt and the two variants simply reflects the fact that the D84E substitution has made the binuclear site more antiferromagnetic, favoring μ-1,3 carboxylate bridges. Thus, the R2-D84E variant could not have changed its bridging to a μ-(1,1)(η^1,η^2) mode, as suggested by the initial crystal structure solution of this variant, as this would produce a ferromagnetic exchange coupling constant (see section III).

In the above VTVH MCD analysis, second-order contributions for R2-D84E have been incorporated via the inclusion of the empirical B-term in the MCD intensity expression (B_i in eq 1). The data can also be fit directly with the spin-Hamiltonian wave functions and the fact that the MCD intensity is proportional to the spin-expectation values of the single iron center being studied by MCD projected onto the dimer states. This complementary fitting approach uses the parameters D_1, E_1, D_2, E_2, J and the effective transition moment products M_{xy}, M_{xz}, and M_{yz} to obtain the best fit (see ref 6 for details). VTVH MCD simulations were performed to map out the solution space. D_1 is the Fe^{II} center for the d → d transition studied by VTVH MCD. A good fit to the VTVH MCD data in Figure 5 collected at 6450 cm^{-1} for the single variant could be obtained only if this transition is associated with the Fe^{II} center with a positive ZFS. This peak can be associated with the 4C Fe^{II} of the binuclear site of the variant. The fit to the VTVH MCD data collected at 6400 cm^{-1} for the double variant matches well with that for the single variant and also can be fit only with a positive D value. However, a fit to the 8800 cm^{-1} transition of the double variant (Figure 6) could be obtained with either a positive or a negative D value.[58] The best fits to the VTVH MCD data are summarized in Table 2.[59]

The spin-Hamiltonian analysis verified that the peak at 6450 cm^{-1} for R2-D84E is best fit with $D_1 = +5$ cm^{-1}, $D_2 = -10$ cm^{-1}, and $J \approx -1.5$ cm^{-1}. In addition, it allowed the 6450 cm^{-1} saturation data to be correlated to the Fe^{II} with a positive ZFS which, from ligand field theory, should be the 4C iron. R2-wt ferrous titration experiments show that the bands at 5500 and 7500 cm^{-1} are associated with the same iron.[6] Spin-Hamiltonian fitting of the VTVH MCD data for the R2-wt at 7500 cm^{-1} shows that this peak corresponds to the Fe^{II} with a positive D, the 4C center.[60]

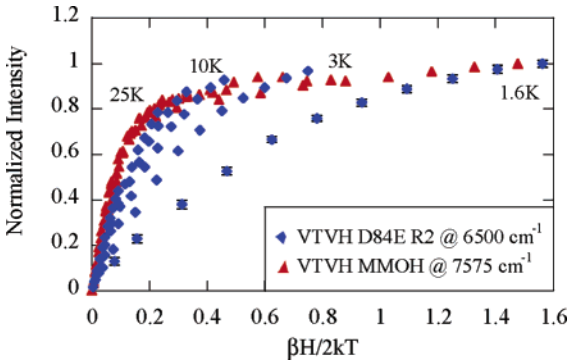

Figure 9. VTVH overlay of the 6450 cm^{-1} band of R2-D84E (blue squares) and the 7575 cm^{-1} band of MMOH (red triangles).

The VTVH data of MMOH and R2-D84E are also dramatically different (Figure 9). VTVH MCD of MMOH saturates very quickly, indicating a large $g_{||}$ value. It was found to have ground state of $M_s = \pm 4$ which is verified by an EPR signal of $g = 16$.[61] This is a ferromagnetic ground state, correlating with a μ-(1,1)(η^1,η^2) bridging carboxylate. In contrast, the VTVH MCD data of R2-D84E saturate more slowly, corresponding to a smaller $g_{||}$ with a larger rhombic splitting. These results reflect the differences in exchange coupling; in fact, upon the D84E substitution, J becomes more negative than the R2-wt, instead of becoming more ferromagnetic to resemble MMOH.

In summary, the D84E variant R2s have different ground and excited states from those of 2-wt. The presence of a 4C Fe^{II} for the variants from the excited-state analysis does not agree with the crystal structure obtained for the single variant, in which a 5C+6C cluster was observed. The weakly antiferromagnetic coupling is also not consistent with the crystallographically detected μ-(η^1,η^2)-carboxylate bridge (vide infra). DFT calculations were pursued to correlate the spectroscopic data with specific structural features.

III. Spectroscopically Calibrated DFT-Derived Model of the Active Site of R2-W48F/D84E and R2-wt. The 93 atom R2-W48F/D84E model was repeatedly geometry optimized using a variety[62] of starting structures. The same optimized structure was obtained in each case, shown in Figure 10, with key bond lengths given in Table 3. This structure has one four-coordinate (4C) and one five-coordinate (5C) iron. Fe1, which is adjacent to E84, singly coordinates E115, H118, and E238 and is chelated in bidentate fashion by E84, resulting in a 5C iron site. Fe2 is 4C, with monodentate coordination to E115, E204, E238, and H241. Note that both E115 and E238 form μ-1,3 carboxylate bridges to the two Fe^{II} ions. This structure

(53) VTVH data taken at 6400 cm^{-1} of the double variant overlay within the standard deviation of the VTVH data taken at 6450 cm^{-1} for the single variant and are included in Supporting Information S2.
(54) Stevens, P. J. *Annu. Rev. Phys. Chem.* **1974**, *25*, 201.
(55) Zhang, Y.; Gebhard, M. S.; Solomon, E. I. *J. Am. Chem. Soc.* **1991**, *113*, 5162−5175.
(56) Schatz, P. N.; Mowery, R. L.; Krausz, E. R. *Mol. Phys.* **1978**, *35*, 1537−1557.
(57) Bennet, D. E.; Johnson, M. K. *Biochim. Biophys. Acta* **1987**, *911*, 71−80.
(58) This is due to the larger error bars associated with the weaker MCD signal of the 8000 cm^{-1} band in Figure 2b.
(59) In the VTVH MCD data for the R2-D84E and R2-W48F/D84E at ~6400 cm^{-1}, the best fit was obtained with an axial, mostly y-polarized transition. However, for the saturation data of the R2-W48F/D84E at 8818 cm^{-1}, equally good fits could be obtained using an axial (z-polarized) or rhombic (y-polarized) model.
(60) Strand, K. R.; Yang, Y. S.; Andersson, K. K.; Solomon, E. I. *Biochemistry* **2003**, *42*, 12223−12234
(61) Hendrich, M. P.; Munck, E.; Fox, B. G.; Lipscomb, J. D. *J. Am. Chem. Soc.* **1990**, *112*, 5861−5865.
(62) These starting geometries included (4C, 4C), (4C, 5C), and (5C, 5C) with E84 and E204 mono- or bidentate and E115 and E238 in μ-1,3 or μ-1,1 bridging geometries.

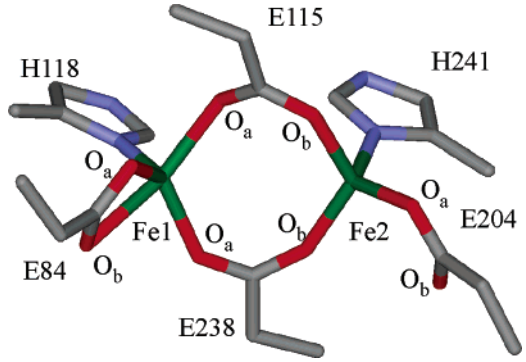

Figure 10. Geometry-optimized structure of R2-W48F/D84E. Hydrogen-bonding (second sphere) residues have been obscured for clarity.

Table 3. Pertinent Bond Lengths from DFT Geometry Optimizations for R2-W48F/D84E and R2-wt ("O$_a$" Refers to the "Top" Carboxylate Oxygen (Closer to E115, See Figure 10) for D/E84 and E204, while for E115 and E238, "O$_a$" Refers to the Carboxylate Oxygen Coordinated to Fe1)

bond	R2-W48F/D84E model	wt 4C+4C model	wt μ-1,1(η^1,η^2) E238 4C+5C model	wt μ-1,3 E238 4C+5C model
Fe1−D/E84 O$_a$	2.12	2.03	1.97	2.07
Fe1−D/E84 O$_b$	2.32	2.52	2.82	2.44
Fe1−E115 O$_a$	2.05	2.11	2.08	2.11
Fe1−H118	1.99	2.07	2.08	2.06
Fe1−E238 O$_a$	1.98	1.95	2.02	1.99
Fe1−Fe2	4.03	4.06	3.73	3.81
Fe2−E115 O$_b$	2.03	2.05	2.11	1.99
Fe2−E204 O$_a$	1.99	1.97	1.93	2.22
Fe2−E204 O$_b$	2.82	2.93	3.19	2.21
Fe2−E238 O$_a$	3.71	3.72	2.38	3.55
Fe2−E238 O$_b$	1.98	2.04	2.25	2.01
Fe2−H241	2.09	2.07	2.11	2.17
ΔE (kcal/mol)		1.0	0.0	0.3

agrees with the CD/MCD spectra of R2-W48F/D84E and the weak AF coupling from the VTVH MCD analysis (vide supra).

Three separate structures of similar energy were obtained for the R2-wt geometry optimizations (Table 3). One (Figure 11a) was 4C+4C with both E115 and E238 bridging in a μ-1,3 mode and D84 and E204 monodentate to Fe1 and Fe2, respectively (H118 coordinates to Fe1 and H241 coordinates to Fe2 to complete binuclear site bonding). The remaining two structures were both 4C+5C with Fe1 4C and Fe2 5C. One structure (Figure 11b and "wt μ-(η^1,η^2) E238 4C,5C model" in Table 3) differs from the 4C+4C structure by having E238 coordinated in a μ-(η^1,η^2) mode, bidentate to Fe2, increasing the coordination number on Fe2 to 5C. D84 and E204 are both monodentate in this structure. The other 4C+5C structure (Figure 11c) has both bridging glutamates (E115 and E238) μ-1,3 coordinated, with D84 monodentate to Fe1 (4C) and E204 bidentate to Fe2 (5C). These structures have similar energies, differing by only 1.0 kcal/mol. This reflects the relatively shallow potential energy surface of the biferrous site with respect to carboxylate coordination, as has been previously described in binuclear iron proteins,[27] model complexes,[63] and DFT calculations.[31,64] The geometric differences among the three models are largely localized to the E238 and E204 residues, the ligands whose coordination modes change between the 4C+4C and the two 4C+5C structures.

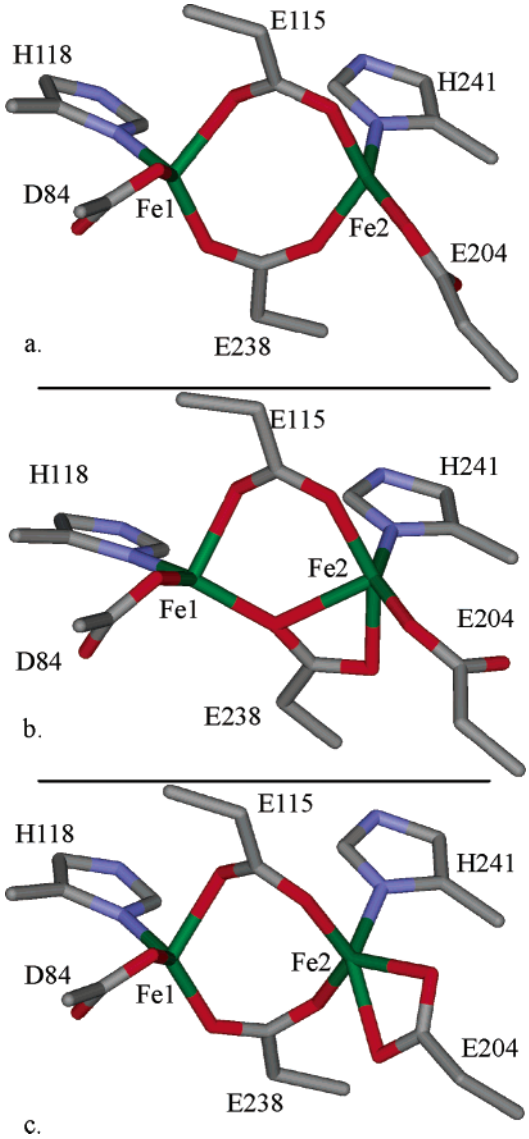

Figure 11. R2-wt DFT geometry-optimized structures. (a) wt 4C+4C structure, (b) wt μ-(η^1,η^2) E238 4C+5C structure, (c) wt μ-1,3 E238 4C,-5C structure. Model hydrogen-bonding (second sphere) residues and hydrogen atoms have been eliminated for clarity.

DFT geometry optimizations based on the R2-W48F/D84E structure identify Fe1 as 5C and Fe2 as 4C, an assignment consistent with the CD/MCD spectroscopy. The structure of wt biferrous R2 is not as easily determined, as the DFT geometry optimizations suggest three possible active-site coordination geometries for the wt active site (Table 3, Figure 11a−c). CD/MCD spectroscopy, which is highly sensitive to the coordination geometry and electronic structure of ferrous iron, found only one species present in biferrous R2-wt. This identifies a limitation in the computational model and requires each structure of similar energy to be compared to spectroscopic observables to determine which is consistent with experimental data. The 4C+4C structure is inconsistent with the MCD spectra, indicating that this structure is not viable at physiological conditions (pH, salinity, etc). The remaining two structures, μ-1,1 E238 and bidentate E204, are 4C+5C where Fe2 is 5C. These are consistent with MCD spectroscopy. The effective swapping of coordination numbers of the Fe sites in R2-wt and R2-W48F/D84E is associated with differing bond lengths and angles to

(63) Lee, D.; Lippard, S. J. *Inorg. Chem.* **2002**, *41*, 2704−2719.
(64) Baik, M. H.; Lee, D.; Friesner, R. A.; Lippard, S. J. *Isr. J. Chem.* **2001**, *41*, 173−186.

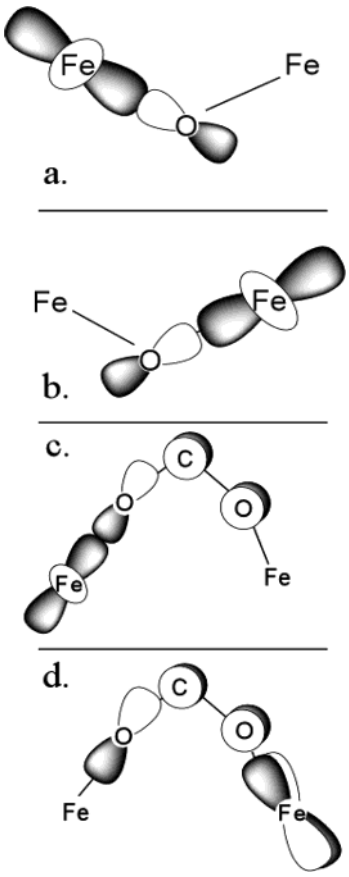

Figure 12. Schematic figure of the orthogonal, ferromagnetic exchange pathways of the μ-1,1 bridging coordination mode (a, b are spin-up and spin-down pairs) and the overlapping, antiferromagnetic exchange pathways of the μ-1,3 bridging mode (c, d are spin-up and spin-down pairs). The μ-1,3 mode has p-overlap with one metal and s-overlap with the other due to the large dihedral angle of bridging (Fe−O−O−Fe = 62°). The orbitals used to construct this figure are found in Supporting Information S5.

the 5C and the 4C ferrous ions of the Fe_2 center. These differences are, in turn, associated with a change in bonding to iron and are reflected in the observed changes in the MCD spectra. Differentiating between the two 4C+5C structures for R2-wt on the basis of the energies of electronic transitions is difficult, as the 5C irons differ only in the identity of the bidentate carboxylate ligand (E238 or E204).

However, the orbital pathways by which the two metal centers can communicate are very different for a μ-(η^1,η^2) bridging carboxylate and a μ-1,3 bridging carboxylate. μ-(η^1,η^2) bridges are observed to lead to ferromagnetic coupling,[65−67] as in biferrous MMO, which has a similar ligand set.[68−71] The major bonding interaction between the iron atoms and the bridging carboxylate oxygen is σ in nature. The oxygen p-orbital on the μ-(η^1,η^2) carboxylate which σ-bonds with a half-occupied orbital on Fe1 (bottom carboxylate in Figure 12a) is oriented perpendicularly to the carboxylate oxygen p-orbital which σ-bonds with the half-occupied orbital on Fe2 (bottom carboxylate in Figure 12b). This type of orthogonal magnetic orbital interaction generally results in ferromagnetic coupling between two metal centers (the Goodenough−Kanamori correlation).[72−74]

In contrast, complexes which have μ-1,3 carboxylate bridges display weak antiferromagnetic coupling, as in several examples from the biferrous binuclear non-heme iron family.[6,9,63,75] The principal interaction between the metal and oxygen atoms in the μ-1,3 bridging geometry is more mixed, but also predominantly σ (80%),[76] with the MO delocalized over the carboxylate such that the same ligand orbitals interact with the half-occupied orbital on both iron centers (top carboxylate in Figure 12c,d). This leads to bonding interactions in which the same O(2p) orbital is involved in both the α- and the β-spin magnetic orbitals (Figure 12c and 12d, respectively). The net result of the coupling via carboxylate orbitals in a bis-μ-1,3 bridged structure would be a weak antiferromagnetic interaction. The coupling in R2-wt is observed spectroscopically to be antiferromagnetic, thus favoring μ-1,3 carboxylate bridging over a μ-(η^1,η^2) carboxylate bridge. Based on the spectroscopy, this indicates that the wt μ-1,3 E238 4C+5C model (Figure 11c) represents the most reasonable structure of R2-wt, with a bidentate E204 ligand as the source of the fifth ligand to Fe2.

In summary, DFT calculations find that the most optimized structure of R2-wt has a monodentate D84 and a bidentate E204 ligand in a 5C+4C geometry and a bidentate E84 with a monodentate E204 ligand in the variant. Note that in the R2-wt structure (Figure 11b) the bond lengths of the bridging oxygen become more inequivalent (stronger to Fe1, weaker to Fe2), this structure becomes more μ-1,3-like and could potentially generate an antiferromagnetic exchange pathway.

Discussion

It was anticipated that the D84E substitution would create an active-site protein environment similar to that of biferrous MMOH and mimic the hydroxylation chemistry.[77] An initial structural report indicated that upon the substitution of Asp84 to Glu84, the structure of the single variant of R2 did in fact resemble MMOH.[21] A second substitution on the W48 residue near the surface resulted in the ability to perform a self-hydroxylation reaction in the presence of oxygen.[19] However, the spectroscopic studies conducted under conditions that more closely resemble the natural environment of R2 did not identify a 5C+6C species with a μ-1,1(η^1,η^2) carboxylate bridge.

I. Correlation of R2-D84E and R2-W48F/D84E to R2-wt. The CD and MCD of both R2-D84E and R2-W48F/D84E gave three peaks in the near-IR region, which can only be satisfactorily fit to a 4C+5C binuclear species. Spin-Hamiltonian analysis of the saturation data of both variants indicates only μ-1,3 carboxylate bridges are present, which is supported by DFT calculations. The geometry-optimized R2-W48F/D84E

(65) Gehring, S.; Haase, W. *Mol. Cryst. Liq. Cryst.* **1989**, *176*, 513−522.
(66) Haase, W.; Gehring, S. *J. Chem. Soc., Dalton Trans.* **1985**, 2609−2613.
(67) Muhonen, H.; Pajunen, A.; Hamalainen, R. *Acta Crystallogr., Sect. B: Struct. Sci.* **1980**, *36*, 2790−2793.
(68) Rosenzweig, A. C.; Frederick, C. A.; Lippard, S. J.; Nordlund, P. *Nature* **1993**, *366*, 537−543.
(69) Assarsson, M.; Andersson, M. E.; Hogbom, M.; Persson, B. O.; Sahlin, M.; Barra, A. L.; Sjoberg, B. M.; Nordlund, P.; Graslund, A. *J. Biol. Chem.* **2001**, *276*, 26852−26859.
(70) Herold, S.; Lippard, S. J. *J. Am. Chem. Soc.* **1997**, *119*, 145−156.
(71) Tolman, W. B.; Liu, S.; Bentsen, J. G.; Lippard, S. J. *J. Am. Chem. Soc.* **1991**, *113*, 152−164.
(72) Blondin, G.; Girerd, J. *Chem. Rev.* **1990**, *90*, 1359−1376.
(73) Goodenough, J. B. *Phys. Rev.* **1955**, *79*, 564.
(74) Kanamori, J. *J. Phys. Chem. Solids* **1959**, *10*, 87.
(75) Reem, R. C.; Solomon, E. I. *J. Am. Chem. Soc.* **1987**, *109*, 1216−1226.
(76) The interaction is complicated by the nonzero torsion angle between the two iron atoms and the carboxylate (φ = 32°), which leads to mixing of the carboxylate in-plane and out-of-plane O(2p) and causes the relationship between the carboxylate orbitals to be less clear in figures 12c and 12d (in contrast with figures 12a and 12b in which the perpendicular orientation of the bridging E238 O(2p) orbitals is well illustrated).
(77) Bollinger, J. M., Jr.; Krebs, C.; Vicol, A.; Chen, S.; Ley, B. A.; Edmondson, D. E.; Huynh, B. H. *J. Am. Chem. Soc.* **1998**, *120*, 1094−1095.

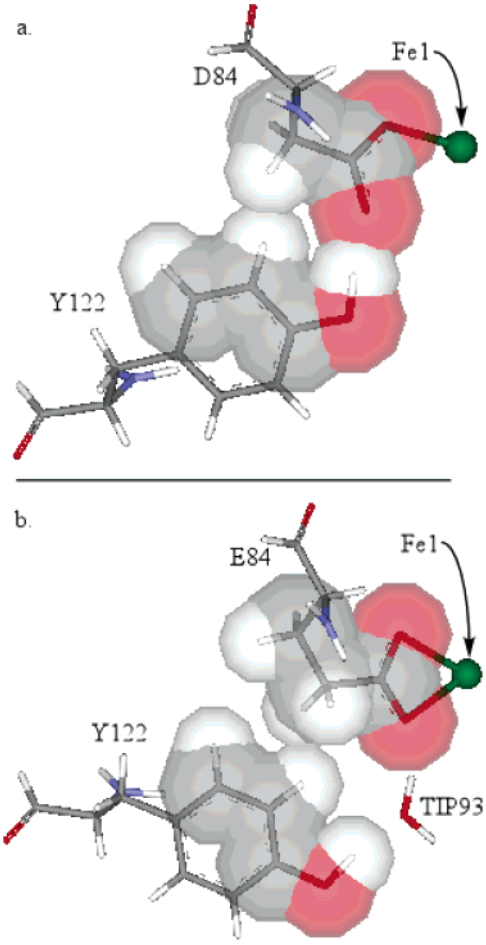

Figure 13. CPK model illustrating the steric interaction between Y122 and D/E84 in (a) wt (ref 35) and (b) D84E/W48F (ref 35) R2. Hydrogen atoms are added to the protein crystal structure by a standard algorithm taking into account atom hybridization, bond order, and formal charges.

structure identifies E84 as a terminal bidentate ligand of Fe1 nearest to Y122, making it 5C, while Fe2 is 4C, with E204 bound in a monodentate fashion. New crystal structures of biferrous R2-D84E and R2-W48F/D84E created under physiological conditions find that both variants are 4C+5C, with two μ-1,3 carboxylate bridges.[35]

The CD spectra of R2-wt and R2-D84E look similar, but low-temperature MCD spectra show a difference in the intensity ratio of the two lower energy peaks associated with the 4C Fe^{II}. Previous studies of the wild-type R2 found that the 5C Fe center was likely to be the one coordinated to E204.[6] DFT calculations performed on the R2-W48F/D84E (vide supra) have indicated that the Fe coordinated to E84 is 5C while the Fe coordinated to E204 is 4C. The different reaction kinetics with O_2[19] are likely to result from the change of the binuclear iron active site from 4C+5C to 5C+4C.

Upon examining the geometry-optimized structures of R2-wt and the R2-W48F/D84E, the major perturbation of the binuclear center is from the D/E84 ligand coordination changing from monodentate to bidentate upon substitution. In R2-wt, the phenolic hydroxy of Y122 hydrogen bonds to O_b of D84 ($O_{Y122}-O_{b,\ D84}$ dist = 2.55 Å), with their R-groups situated with near-van der Waals radius separation ($r(C_{\beta D84} - C_{\delta' Y122}) = 3.60$ Å) (Figure 13a). When aspartate is substituted with glutamate, the lengthening by one methylene ($-CH_2-$) unit results in a 1 Å shift of the phenolic hydroxy group of Y122 away from Fe1

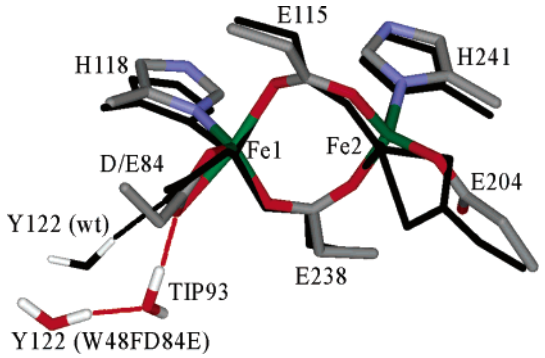

Figure 14. Overlay of the geometry-optimized R2-W48F/D84E (color) and R2-wt μ-1,3 E238 4C+5C (black) models illustrating the geometric change upon mutation. Hydrogen bonds are shown as dashed lines. Y122-(wt) (black) and Y122(W48F/D84E) (red) are modeled by water in the calculation.

and breaks the hydrogen bond between the uncoordinated carboxylate oxygen atom of D84 (corresponding to $O_{b,D84}$ in our calculations) to the phenolic hydroxy group of Y122. This appears to be the source of the geometric change from biferrous R2-wt, resulting in a greater steric repulsion between E84 and Y122 (Figure 13b), and preventing the close alignment observed in R2-wt. Closer examination of the interaction between the E84 carboxlate and Y122 hydroxy termini finds that breaking the hydrogen bond between Y122 and O_b of D84 ($r(O_{Y122}-O_{b,D84}) = 4.67$ Å) creates a small cavity between the two R-groups into which a water, TIP93 (Figure 13b), can insert, forming hydrogen bonds with both $O_{b,D84}$ ($r(O_{TIP93}-O_{b,D84}) = 2.83$ Å) and O_{Y122} ($r(O_{TIP93}-O_{Y122}) = 2.59$ Å).[78] Another effect of the steric interaction between Y122 and E84 is to push Y122 down and away from the Fe^{II} center, and, more importantly for this study, shift E84 toward Fe1. This results in the geometric change observed on Fe1 from 4C to 5C as D/E84 changes from monodentate to bidentate coordination. This changes the bonding to the bridging carboxylates, E115 and E238, rotating the Fe$-O_{a,E115}$ and Fe$-O_{a,E238}$ bonds (O_a is the carboxylate oxygen of E115 and E238 coordinated to Fe1). This, in turn, propagates to Fe2, resulting in E204 changing from bidentate to monodentate, and generating the observed 5C+4C Fe^{II} coordination geometry in R2-W48F/D84E (Figure 10). An overlay of the geometry-optimized R2-W48F/D84E (color) and wt μ-1,3 E238 4C+5C (black) DFT models is shown in Figure 14.

II. Differences between R2-D84E and MMOH. Although R2-D84E, R2-W48F/D84E, and MMOH form peroxo intermediates, it should be emphasized that these R2 variants and R2-wt react with oxygen 3 orders of magnitude faster than MMOH in the absence of MMOB.[77,79] In addition, changes to R2 at the iron center which do not match the ligand set of MMOH (for example, E238A/Y122F) have resulted in self-hydroxylation.[25,80] This indicates that a range of structural modifications on the

(78) It should be noted that the steric interaction between Y122 and E84 is not required in the geometry optimizations to reproduce the bidentate coordination of E84 to Fe1 (Figure 10). The model used for the R2-W48F/D84E active site replaces the Y122 residue with a water molecule where C is modeled by a hydrogen (with its coordinates frozen during the optimizations) and O as the water oxygen (also frozen during optimization). Thus, there is no phenyl ring present to interact with the aliphatic chain of E84, although the effects of this interaction, the addition of TIP93 and the displacement of Y122 relative to wt, are included.

(79) Liu, K. E.; Nesheim, J. C.; Lee, S.-K.; Lipscomb, J. D. *J. Biol. Chem.* **1995**, *270*, 24662−24665.
(80) Ormo, M.; deMare, F.; Regnstrom, K.; Aberg, A.; Sahlin, M.; Ling, J.; Loehr, T. M.; Sanders-Loehr, J.; Sjoberg, B. M. *J. Biol. Chem.* **1992**, 267.

Table 4. Distances from the Core to Either the α Carbon or the Carboxylate Carbon

α Carbon

	MMOH	D84E R2	wt R2	
GLU243	5.6	4.8	4.6	GLU238
GLU114	5.8	6.2	5.7	GLU84/ASP84
GLU144	5.3	4.8	4.7	GLU115
HIS147	6.7	6.9	6.9	HIS118
GLU209	6.9	6.4	6.4	GLU204
HIS246	6.6	6.6	6.6	HIS241

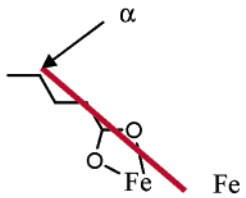

γ carbon

	MMOH	D84E R2	wt R2	
GLU243	3.2	2.3	2.1	GLU238
GLU114	4.6	4.1	4.1	GLU84/ASP84
GLU144	2.6	2.3	2.1	GLU115
HIS147	n/a	n/a	n/a	HIS118
GLU209	4.2	4.4	4.5	GLU204
HIS246	n/a	n/a	n/a	HIS241

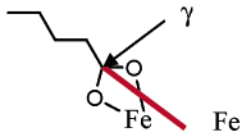

R2 iron center can result in two-electron oxidation, but do not necessarily make the biferrous core similar to MMOH.

The new set of wt and single variant crystal structures shows dramatic changes when compared to previous crystal structures obtained for the R2-wt and R2-D84E. The different preparation methods that were explored using CD/MCD found no changes, suggesting that the conditions used to crystallize the enzyme may not lead to the dominant lowest energy configuration.[35] Both CD/MCD spectroscopy and the new set of crystal structures show that the R2-D84E substitution does not create a site which reproduces the structure of MMOH. Three possibilities for the differences in ligation between MMOH and R2-D84E are considered: coordination of water, protein constraints, and relative size of water pockets.

i. Coordination of Water. One biferrous R2 structure, that of R2-D84E,[21] identifies a coordinated water molecule bridging the two ferrous ions, with $r(\text{Fe1}-\text{O}_{\text{wat}}) = 2.9(1)$ Å and $r(\text{Fe2}-\text{O}_{\text{wat}}) = 2.3(1)$ Å. This structure reproduced the coordination geometry in MMOH with E238 μ-(η^1,η^2) and E204 monodentate coordinated. A DFT geometry optimization was performed using this geometry as a starting point, including the same set of hydrogen-bonding analogues described above for the R2-W48F/D84E variant. In the optimized biferrous structure, E238 changed from a μ-1,1(η^1,η^2) to a μ-1,3 bridging coordination geometry, while E204 remained monodentate (coordinates and structure in Supporting Information S3), suggesting that the addition of this bound water is not sufficient to reproduce the MMOH active site. Additionally, each of the biferrous MMOH crystal structures[22] identifies a water coordinated to Fe1 in a nonbridging mode trans to E144 (equivalent of E115 in R2) (Figure 1C). This water molecule hydrogen bonds to both the noncoordinated oxygen of the carboxylate on the adjacent E114 residue (D84 in R2-wt) and the bridging oxygen of the μ-1,1-(η^1,η^2) bridging E243 residue (E238 in R2-wt). A geometry optimization was performed on a model using the R2-W48F/D84E variant protein constraints and orienting the coordinating ligands to best reflect the positions of the equivalent ligands in MMO. This optimization again leads to a change in E238 from μ-1,1(η^1,η^2) to μ-1,3 coordination, while the water remains coordinated to Fe1 and hydrogen bonded to both the adjacent E238 carboxylate oxygen and the noncoordinated oxygen of the E84 carboxylate (coordinates and structure in Supporting Information S3).

ii. Protein Constraints. A major difference between the R2-D84E and MMOH active-site structures is in the iron−iron distances which may either cause or result from a μ-1,1 or μ-1,3 bridging carboxylate. The iron−iron distances over the series of biferrous R2-wt,[20] R2-D84E,[35] and MMOH[22] are 3.9, 3.9, and 3.4 Å, respectively. E243 in MMOH bridges in μ-1,1(η^1,η^2) fashion bidentate to Fe2, while E238 bridges in μ-1,3 fashion in both R2 variants. One possibility is that the two irons in the binuclear site are held apart by the protein backbone in R2. However, comparing the distances of the α and γ carbons to the iron center (Table 4) indicates that the volume spanned by the six α carbons is greater in MMOH than in R2-D84E, mostly due to the E243 and E144 (E238 and E115 in R2) α carbons residing further from the Fe2 center in MMOH. The greater distance from the core of the α carbon of E243 in MMOH relative to the α carbon of E238 in R2-D84E (0.8 Å further) could promote the observed μ-(η^1,η^2) coordination mode. However, this is not observed in E144, which has a μ-1,3 bridging mode despite an equally long α carbon distance in comparison to E115 in R2-D84E. The E84 in R2-D84E and E144 in MMOH have similar differences in distance, but in opposite directions, so they are also unlikely to play a role in the decreased Fe−Fe distance. Thus, the constraints from the central set of ligands are not a main factor in determining coordination mode.

iii. Relative Pocket Size. The binuclear active sites of both MMOH and R2-D84E are situated in similar four α-helix bundles, but there are notable differences in the second-coordination-sphere residues. The O_2/substrate binding pocket of MMOH is large (~7 Å from the Fe2 center to F188 and F192 on the opposite side (Figure 15, top)) and contains much water. In R2-wt and R2-D84E, the O_2 binding pocket is much smaller with F208 located only 3.5 Å from the Fe2 site (Figure 15, bottom). This difference in the protein structure adjacent to the binuclear iron center changes the steric and electrostatic

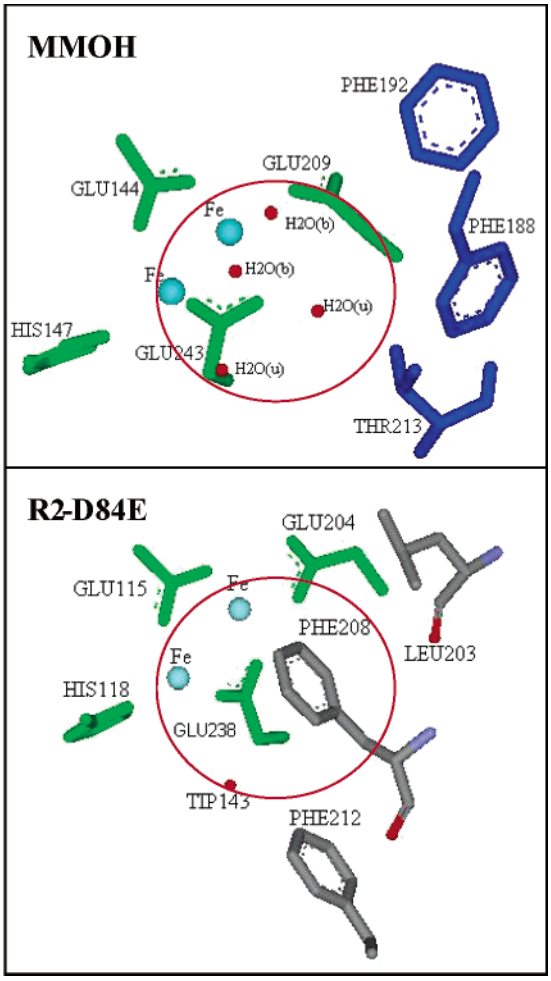

Figure 15. Pocket in MMOH (top) and R2-D84E (bottom). Core ligands are in green, the binuclear site is light blue, water is in red, and second sphere residues are blue for MMOH and grey for R2-D84E. Water is labeled in MMOH as bound (b) or unbound (u).

interactions experienced by coordinating residues, especially E238 (the equivalent residue is E243 in MMOH). In R2, the orientation of E238 is sterically constrained by adjacent F208 and F212 residues, while in MMOH, these interactions are not present, leading to different orientations of E238/E243 in the two proteins. It is interesting to note that the binding of the effector protein MMOB to MMOH is known to perturb the active site, as there are spectral and reduction potential changes at the diiron center upon binding of MMOB.[52,81] Crystallographic studies have proposed that the active-site pocket in MMOH is a possible MMOB binding site.[22] Such an interaction would be anticipated to change the geometric and electronic structure of the binuclear ferrous site of MMO relative to the crystallized MMOH form and contribute to its increased reactivity.

(81) Gassner, G. T.; Lippard, S. J. *Biochemistry* **1999**, *38*, 12768−12785.

Summary

The spectroscopic methodology and calculations applied in this study have provided detailed insight into the binuclear iron active sites of reduced D84E and W48F/D84E variants of R2. CD/MCD studies have shown that the reduced variant proteins have a 5C+4C site weakly antiferromagnetically coupled through μ-1,3 carboxylate bridges. DFT calculations have explored different geometries of the binuclear site and have designated a structure which correlates with spectroscopy. This structure assigns the Fe1 (which is bound bidentate by E84 adjacent to Tyr122 which is oxidized) as 5C and the other iron as 4C. This is in contrast with R2-wt, which is 4C+5C with Fe2 as the 5C center. The geometric and electronic structures of the single and double variants were evaluated and found to be dissimilar to MMOH in coordination, geometry, and mode of bridging. DFT calculations have eliminated the possibility of coordinating water as the main contributor to the difference in coordination. It is also unlikely that protein constraints position the iron distances. A possible cause of the difference in the μ-1,1 versus μ-1,3 bridging of E243/E238 between MMOH and R2-D84E is the presence of second sphere residues in the latter which have different packing orientations that block channels for water and other small molecules. Thus, although the central ligand set is the same in MMOH and R2-D84E, the protein environment plays a major role in structuring the active site, as the iron centers in the single and double variants resemble that in R2-wt more than that in MMOH.

Acknowledgment. We thank Dr. Yi-Shan Yang for helpful discussions and preliminary studies. We acknowledge financial support by the NSF-Biophysics Program Grant MCB 9816051 (E.I.S.), NSF GM55365 (J.M.B., Jr.), and NSF Pre-Doctoral Fellowship to P.-p.W.

Supporting Information Available: Active-site model of R2-wt; VTVH MCD data of R2-D84E overlaid with R2-W48F/D84E; coordinates from DFT geometry optimization of R2-W48F/D84E; chemically reduced R2-wt versus Fe(II) loaded R2-wt; and magnetic orbitals (E238) of R2-wt DFT optimized geometry structures (PDF). This material is available free of charge via the Internet at http://pubs.acs.org.

JA0374731